Optimal sediment transport for morphodynamic model validation

Bosboom, J.; Mol, M.; Reniers, A. J.H.M.; Stive, M. J.F.; de Valk, C. F.

DOI
10.1016/j.coastaleng.2020.103662

Publication date
2020

Document Version
Final published version

Published in
Coastal Engineering

Coastal Engineering 158 (2020) 103662

Contents lists available at ScienceDirect

Coastal Engineering

journal homepage: www.elsevier.com/locate/coastaleng

Optimal sediment transport for morphodynamic model validation

J. Bosboom [a,*], M. Mol [b], A.J.H.M. Reniers [a], M.J.F. Stive [a], C.F. de Valk [c]

[a] Faculty of Civil Engineering and Geosciences, Delft University of Technology, Department of Hydraulic Engineering, P.O. Box 5048, 2600 GA Delft, The Netherlands

[b] MIcompany, Vijzelstraat 72 - floor 7A, 1017 HL Amsterdam, The Netherlands

[c] Royal Netherlands Meteorological Institute (KNMI), P.O. Box 201, 3730 AE De Bilt, The Netherlands

ARTICLE INFO

Keywords:
Root-mean-squared error
Model accuracy
Morphodynamic modelling
Model validation
Optimal transport
Monge–Kantorovich
Root-mean-squared transport error
Effective transport difference

ABSTRACT

Although commonly used for the validation of morphological predictions, point-wise accuracy metrics, such as the root-mean-squared error (RMSE), are not well suited to demonstrate the quality of a high-variability prediction; in the presence of (often inevitable) location errors, the comparison of depth values per grid point tends to favour predictions that underestimate variability. In order to overcome this limitation, this paper presents a novel diagnostic tool that defines the distance between predicted and observed morphological fields in terms of an optimal sediment transport field, which moves the misplaced sediment from the predicted to the observed morphology. This optimal corrective transport field has the "cheapest" quadratic transportation cost and is relatively easily found through a parameter-free and symmetric solution procedure solving an elliptic partial differential equation. Our method, which we named effective transport difference (ETD), is a variation to a partial differential equation approach to the Monge–Kantorovich L^2 optimal transport problem. As a new error metric, we propose the root-mean-squared transport error (RMSTE) as the root-mean-squared value of the optimal transport field. We illustrate the advantages of the RMSTE for simple 1D and 2D cases as well as for more realistic morphological fields, generated with Delft3D, for an idealized case of a tidal inlet developing from an initially highly schematized geometry. The results show that by accounting for the spatial structure of morphological fields, the RMSTE, as opposed to the RMSE, is able to discriminate between predictions that differ in the misplacement distance of predicted morphological features, and avoids the consistent favouring of the underprediction of morphological variability that the RMSE is prone to.

1. Introduction

Quantitative validation methods for morphological predictions are often grid-point based: they compare observations and predictions per grid-point and compute various metrics for the entire set or subset of grid-points. Accuracy metrics, e.g. the root-mean-squared error (RMSE) or the mean absolute error (MAE) measure the averaged correspondence between individual pairs of model outcomes and observations, whereas skill metrics determine the accuracy, using an accuracy metric of choice, relative to the accuracy of a prediction produced by a standard of reference (Gallagher et al., 1998). Several morphological studies rely solely on a skill score, most notably a mean-squared-error skill score (MSESS or BSS, Sutherland et al., 2004; Bosboom et al., 2014) as a performance metric (e.g. van Rijn et al., 2003; Plant et al., 2004; Henderson et al., 2004; Pedrozo-Acuña et al., 2006; Scott and Mason, 2007; Ruggiero et al., 2009; Orzech et al., 2011; Walstra et al., 2012; Williams et al., 2012; Simmons et al., 2017; Monge-Ganuzas et al., 2017; Luijendijk et al., 2017, 2019). In other cross-shore, longshore and area modelling studies, skill scores and accuracy metrics are used in concert (e.g. Ruessink et al., 2007; Dam et al., 2016; Fortunato et al., 2014; Simmons et al., 2019). These procedures are sometimes supplemented with bias- and correlation-based measures, either directly (e.g. Gallagher et al., 1998; Roelvink et al., 2009; McCall et al., 2010, 2015; Ganju et al., 2011; Davidson et al., 2013; Dodet et al., 2019; Hallin et al., 2019) or through the Murphy–Epstein decomposition of the MSESS (Sutherland et al., 2004; Bosboom and Reniers, 2018), which additionally employs an amplitude error (e.g. Sutherland et al., 2004; Ruessink and Kuriyama, 2008; van der Wegen et al., 2011; van der Wegen and Roelvink, 2012; Elmilady et al., 2019).

The various statistical measures condense a large number of data into a single value, inevitably emphasizing only certain aspects of the quality of the model results. Morphodynamic modellers are inclined to judge model results on the reproduction of patterns. Unfortunately, point-wise accuracy and derived skill metrics tend to penalize, rather

* Corresponding author.
E-mail address: j.bosboom@tudelft.nl (J. Bosboom).

https://doi.org/10.1016/j.coastaleng.2020.103662
Received 5 June 2019; Received in revised form 11 December 2019; Accepted 2 February 2020
Available online 6 February 2020

than reward, the model's capability to provide information on features of interest, such as scour holes, accumulation zones and migrating bars or tidal channels (Bosboom et al., 2014; Bosboom and Reniers, 2018). This tendency to reward the underestimation of variability (Anthes, 1983; Arpe et al., 1985; Taylor, 2001) is easily illustrated by the classical example of the "double penalty effect" (Bougeault, 2003): a prediction, which reproduces a feature at the wrong location, is penalized twice, both where the predicted feature is and where it should be, and is thus diagnosed with a twice as large mean-squared error (MSE) as a flat bed prediction. More in general, for a nonperfect correlation, as would be the case in the presence of location errors, accuracy as well as skill values can be "improved" by underestimation of the variability (Bosboom et al., 2014; Bosboom and Reniers, 2018). Clearly, this is inconsistent with the common judgement of morphologists. In order to avoid the underestimation of bed changes, an indicator should be added to determine whether the predicted variance is close to the observed variance. Further, since point-wise metrics do not take the spatial ordering of grid-points into account, they are not sensitive to misplacement distance. The simplest demonstration of the latter is a prediction of a feature on a otherwise flat bed that has been misplaced over a distance larger than its size. For this situation, metrics that impose a penalty on point-wise bed level differences yield identical values irrespective of the misplacement distance.

The above illustrates the need for new validation metrics that account for the spatial structure of morphological fields. Pioneering techniques in the field of weather forecasting comprise field deformation methods, which give information about how much the predicted field needs to be manipulated spatially (displacement, rotations, scaling, etc.) and quantify the residual errors (Gilleland et al., 2009). Bosboom and Reniers (2014b) developed a field deformation or image warping approach for morphological model validation that determines a smooth displacement field between morphological predictions and observations minimizing the residual point-wise error and computes domain-averaged errors based on the displacement as well as residual error fields. The method includes a robust and physically intuitive combined error metric, the $RMSE_w$, which rewards predictions to the degree that a larger error reduction can be obtained with smaller displacements. This error metric for morphological model validation results in choices as to which of two predictions is better that are consistent with visual validation, demonstrating the potential of field deformation methods to overcome the limitations of point-wise metrics. However, the so-determined optimal smooth transformation merely relocates predicted bed levels in the two-dimensional domain. As a result, horizontal dimensions of features may get distorted, such that sediment is not necessarily conserved.

For morphodynamic model validation, it seems more natural to base a validation metric on a transformation between predictions and observations defined in terms of the physical quantity responsible for morphodynamic development: sediment transport. Therefore, we have developed a method that determines the distance between morphological fields in terms of the minimal sediment transport required to change the one field into the other. Since the transformation is defined in terms of sediment transport, mass will now be conserved, but features may not. The optimal transformation or effective transport difference (ETD) has the "cheapest" transportation cost and is relatively easily found by solving an elliptic partial differential equation. The solution procedure is parameter-free and symmetric, the optimal transport field from observations to predictions being the inverse of the optimal transport field from predictions to observations. The new domain-averaged error metric that we propose is a multiple of the minimum transportation cost.

Our ETD method is related to the Monge–Kantorovich theory of optimal mass transport, which deals with the transport of a distribution of mass to another distribution of mass on the same space, in such a way as to keep the transportation cost to a minimum. The first formulation of the optimal mass transport problem was due to Monge in 1781, who considered the most economical way of transporting a pile of soil for construction works from one site to another. Monge used a cost function equal to the norm of the distance, based on the argument that the cost of transportation of an individual mass is proportional to its weight times the travelled distance (Rachev and Rüschendorf, 1998). This leads to the physical interpretation of the L^1 optimization, which minimizes the norm, in terms of the minimization of work, assuming that the work of transporting a mass element Δm over a distance Δd is $\Delta m \Delta d$ (Bogachev and Kolesnikov, 2012).

The work of Kantorovich in 1948 gave the optimal mass transport problem its modern, generalized formulation, which is today known as the L^p Monge–Kantorovich problem (Villani, 2003). Here one is allowed to "divide grains", whereas in Monge's formulation grains that share the same initial location must also share the same final location (Rachev and Rüschendorf, 1998). Especially the L^2 Monge–Kantorovich problem, which minimizes the squared norm of the distance, has been researched intensively by theoretical mathematicians (Villani, 2003), since, as opposed to the L^1 problem, it allows for relatively simple solutions. The search for efficient numerical solvers has only recently become a lively research domain (Santambrogio, 2015). Benamou and Brenier (2000) and Benamou et al. (2002) were the first to construct a robust and efficient numerical solver for the L^2 Monge–Kantorovich problem by introducing a partial differential equation approach. In a fluid mechanics framework, they showed that the L^2 optimal transport is equivalent to minimizing a kinetic energy functional among solutions of the continuity equation, with the optimal solution given as the gradient of a potential and, thus, being irrotational.

Our ETD method also employs an irrotationality condition for the optimal transport in order to reformulate a transport optimization problem in terms of a partial differential equation that is easily solved. However, whereas the L^2 Monge–Kantorovich problem penalizes the quadratic distance the transformation moves each bit of material, weighted by the material's mass, our quadratic cost function penalizes the squared sediment transport, i.e. mass times distance, herewith retaining the original physical Monge's interpretation in terms of work, albeit in a quadratic sense. New aspects are further that our model boundaries are open to sediment, which allows a bias to exist between the two bathymetric fields.

This paper presents a novel error metric, the root-mean-squared transport error (RMSTE) as a multiple of the "cheapest" quadratic cost for the transportation of sediment from predictions to observations and establishes its applicability for morphodynamic model validation. In doing so, for fairness of comparison, the behaviour of the RMSTE as an error metric is evaluated in comparison to the behaviour of its point-wise counterpart, the RMSE. First, in Section 2, we describe our ETD method of finding the optimal transport difference between two morphological fields, leading to the formulation of the RMSTE. Section 3 shows in 1D how the RMSTE and RMSE behave for both misplaced features and features that are underestimated in size. Further, it compares the RMSTE and RMSE for a 2D example, in which the latter of these two metrics suffers from the double penalty effect. Next, in Section 4, we put the RMSTE to a more realistic test using morphological fields, generated with Delft3D, for an idealized case of a tidal inlet developing from an initially highly schematized geometry. This section not only compares the RMSTE to the RMSE but to the $RMSE_w$ as well. The implications of the results for morphodynamic model validation are discussed in Section 5. Section 6 concludes with a summary of our findings and identifies future work.

2. A new method

In this section, we present a new error metric, the RMSTE, which measures the mismatch between two morphological fields in terms of sediment transport. First, Section 2.1 describes common error metrics,

such as the RMSE, that penalize bed level differences between predictions and observations. Second, in Section 2.2, we define the RMSTE as (a multiple of) the optimal (i.e. minimum) quadratic transport cost required to transform the predictions into the observations. Third, Section 2.3 demonstrates that the optimal transport, on which RMSTE is based, can be found by solving an elliptic partial differential equation. Finally, Section 2.4 briefly describes the numerical implementation.

2.1. Penalty on bed level differences

More traditional error metrics are based on a point-wise comparison of predictions and observations. Let h_1 and h_2 be the predicted and observed bed levels above a certain vertical reference level, respectively, for a set of points $\mathbf{x}$ over a domain Ω. If $e = h_2 - h_1$ is the point-wise bathymetric error, the p-norm bathymetric error is defined as:

$$\|e\|_p = \left(\int_{\mathbf{x}\in\Omega} |e|^p \mathrm{d}\mathbf{x} \right)^{1/p} \tag{1}$$

with $p = 1, 2, \infty$ the usual choices for p and the $p = 2$ norm known as the *Euclidean norm*. Often used point-wise accuracy metrics, the mean absolute error (MAE) and the RMSE are constant multiples of the 1-norm and 2-norm errors, respectively. The RMSE reads:

$$\mathrm{RMSE} = \frac{1}{\sqrt{A_\Omega}} \left(\int_{\mathbf{x}\in\Omega} |h_2(\mathbf{x}) - h_1(\mathbf{x})|^2 \mathrm{d}\mathbf{x} \right)^{1/2} = \frac{1}{\sqrt{A_\Omega}} \|e\|_2 \tag{2}$$

with A_Ω the domain surface area. The MSE simply is the square of the RMSE.

Note that in Sections 3 and 4, we have chosen to visually compare predictions and observations by means of difference fields $\delta = h_1 - h_2$ rather than error fields e. The advantage of defining the deviations as predicted values minus real, observed values is that the observations are the reference point from which the predictions may differ, such that a positive deviation indicates an overprediction and a negative deviation an underprediction. Of course, the RMSE is unaffected when computed from difference fields δ rather than from e.

2.2. Penalty on transport magnitude

Assume that $\mathbf{q}$ on Ω represents a cumulative, depth-integrated transport of sediment from h_1 to h_2, such that with a constant grain size and porosity, and, hence, constant density, the sediment volume balance is satisfied:

$$\nabla \cdot \mathbf{q} = h_1 - h_2 \tag{3}$$

with $\nabla\cdot$ is the divergence operator and either known or unknown transports normal to the boundary $\partial\Omega$ of Ω at every point of $\partial\Omega$. Note that $\mathbf{q}$ is to be interpreted as a corrective transport field moving sediment from the predicted morphology h_1 to the observed field h_2, and, hence, as a transport difference field between h_1 and h_2.

There may exist a multitude of transport fields satisfying Eq. (3). An *optimal* field can be determined by minimizing the p-norm of the transport field:

$$\underset{\mathbf{q}}{\text{minimize}} \quad \|q\|_p = \left(\int_{\mathbf{x}\in\Omega} |\mathbf{q}(\mathbf{x})|^p \mathrm{d}\mathbf{x} \right)^{1/p} \tag{4}$$

with $q = |\mathbf{q}|$ is the magnitude of the transport field.

Eq. (4) under the constraint Eq. (3) differs from the L^p Monge–Kantorovich mass transfer problem (Villani, 2003) in that it minimizes the cumulative transport, and thus, assuming constant density, mass times distance, to the power p, rather than the travelled distance to the power p, weighted by the amount of transferred mass. If the exponent $p = 1$, the minimization problem of Eqs. (3) and (4) reduces to an L^1 Monge–Kantorovich problem with the Euclidean distance as the cost function (Evans, 1997). Numerical methods for solving this problem exist (Benamou and Carlier, 2015), but are considerably more complex than the solution of Eqs. (3) and (4) with $p = 2$. As we will see in Section 2.3, the case $p = 2$ is relatively easily solved by rewriting the optimality condition Eq. (4) and will therefore be the one used in this paper.

Summarizing, we will solve the following L^2 problem minimizing a quadratic transport cost:

$$\begin{aligned} \underset{\mathbf{q}}{\text{minimize}} \quad & \|q\|_2 = \left(\int_{\mathbf{x}\in\Omega} |\mathbf{q}(\mathbf{x})|^2 \mathrm{d}\mathbf{x} \right)^{1/2} \\ \text{subject to} \quad & \nabla \cdot \mathbf{q} = h_1 - h_2. \end{aligned} \tag{5}$$

By rewriting the cost functional, Eq. (5) can be reformulated as an elliptic partial differential equation from which the quadratic optimal transport field $\mathbf{q}_{L2}$ is relatively easily solved (see Section 2.3). In analogy with Eq. (2), we can now introduce the RMSTE as:

$$\mathrm{RMSTE} = \left(\frac{1}{A_\Omega} \int_{\mathbf{x}\in\Omega} |\mathbf{q}_{L2}(\mathbf{x})|^2 \mathrm{d}\mathbf{x} \right)^{1/2} = \frac{1}{\sqrt{A_\Omega}} \|\mathbf{q}_{L2}\|_2. \tag{6}$$

Note that since Eq. (6) is a constant multiple of the optimal quadratic transport cost, the triangle inequality[1] is satisfied; there is no other transport field satisfying Eq. (3) and the boundary conditions that obtains a lower RMSTE than $\mathbf{q}_{L2}$.

The RMSTE, Eq. (6), can be seen to penalize the transport itself, while the RMSE, Eq. (2), penalizes the bed level changes and thus, according to Eq. (3), the divergence of the transport. As a measure of volume times displacement per unit surface area, the RMSTE has units m^2, while the RMSE, which measures a volume per unit surface area, has units m.

Redistributing sediment from h_1 to h_2 through $\mathbf{q}_{L2}$ implies removing sediment at locations for which $\delta = h_1 - h_2 > 0$ and adding sediment at locations for which $\delta = h_1 - h_2 < 0$. We can express the sediment surplus as an excess height,[2] given by $\delta_1 = \max(\delta, 0)$ and the sediment shortage as a deficit height (see Footnote 2) given by $\delta_2 = \max(-\delta, 0)$. Of course, in Eq. (3) $h_1 - h_2 = \delta_1 - \delta_2$. With these definitions, RMSTE can be seen to measure the smallest overall volume transport of sediment required to excavate δ_1 and fill δ_2. For a zero bias between predictions and observations and boundaries closed for sediment, δ_1 will be transported to δ_2. More in general, sediment may also be added or removed through the boundaries depending on the transportation cost.

2.3. Solving the effective transport difference

The solution of Eq. (5) proves to be irrotational (see Appendix) and can therefore be represented as the gradient of a scalar field, the potential ϕ:

$$\mathbf{q}_{L2} = \nabla\phi. \tag{7}$$

With Eq. (7), Eq. (3) can be written as:

$$\nabla^2\phi = h_1 - h_2. \tag{8}$$

Eq. (8) is a standard Poisson equation for which numerous efficient solvers are available. With ϕ defined through Eq. (7), this Poisson equation is fully equivalent to Eq. (5). This realization is analogous to the interpretation of Moser's coupling in terms of optimization theory in Brenier (2003, Section 2.6), where it is shown that the solution to a variant to the L^2 Monge–Kantorovich problem can be represented as a potential flow satisfying the Laplace equation.

[1] A function $m(A, B)$ is a metric if it is symmetric $m(A, B) = m(B, A)$, positive-definite $m(A, B) \geqslant 0$ and $m(A, B) = 0 \Leftrightarrow A = B$, and satisfies the triangle inequality $m(A, B) + m(B, C) \geqslant m(A, C)$. Both the RMSE and the RMSTE satisfy these criteria.

[2] Surplus or shortage volume (m^3) per squared metre of domain area (m^2), hence an excess or deficit height (m).

The two typical boundary conditions for our application are:

1. Neumann-type boundary condition for a boundary *closed* for sediment:

$$\mathbf{q} \cdot \mathbf{n} = \nabla\phi \cdot \mathbf{n} = 0 \tag{9}$$

for all points on the boundary $\partial\Omega$. Here $\cdot$ denotes the inner product and the normal vector $\mathbf{n}$ is the unit vector that is perpendicular to the surface $\partial\Omega$ and points outwards from $\partial\Omega$.

2. Dirichlet-type boundary condition for a *free* boundary that allows for sediment transport across the boundary:

$$\phi = 0 \tag{10}$$

for all points on the boundary $\partial\Omega$, which signifies that there is no constraint on $\mathbf{q}$ on the boundary (see Appendix).

One can prove that for the case of Dirichlet boundary conditions the solution to Poisson's equation always exists and is unique. The same holds for combination boundary conditions, which consist of Dirichlet boundary conditions on part of the domain boundary and Neumann boundary conditions on the remainder of the domain boundary. For the case of Neumann boundary conditions, a solution only exists if the transport $\nabla\phi \cdot \mathbf{n}$ integrated over the boundary $\partial\Omega$ is consistent with $h_1 - h_2$ integrated over Ω. Then the solution is unique up to an overall additive constant. Clearly, it is sufficient to determine ϕ up to an arbitrary additive constant, which has no impact on the value of the sediment transport $\mathbf{q} = \nabla\phi$.

The above implies that if all boundaries are closed to sediment, the condition for existence of a solution to Eq. (8) is that the domain-averaged value of the right-hand-side $h_1 - h_2$ equals zero. The term $h_1 - h_2 = \delta_1 - \delta_2$ was seen to act as a source and sink term, with δ_1 the excess height, which needs to be removed, and δ_2 the deficit height, which needs to be supplied (see Section 2.2). If its domain-averaged value is equal to zero, hence, in the absence of a bias, the excess sediment δ_1 suffices to fill the sediment deficit δ_2, such that a solution can be found within the domain. If its domain-averaged value is unequal to zero, i.e. in the case of a bias, a net sediment import or export is required to obtain a match between predictions and observations. Then, at least one free boundary condition should be applied.

In specifying the boundary conditions for a particular application, one must bear in mind that $\mathbf{q}$ represents the optimal cumulative transport through which a perfect match is obtained between predictions and observations, hence a transport difference or error. This error is just as arbitrary on the boundary as within the domain, such that in general $\mathbf{q} \cdot \mathbf{n}$ on the boundary $\partial\Omega$ is unknown and there should be no constraint on $\mathbf{q}$ on the boundary. This means that from a physical point of view, *free* boundaries, which are part of the transport optimization, are generally the logical choice. Only in the special case of a boundary that is physically closed for sediment, one may assume that the error $\mathbf{q}\cdot\mathbf{n}$ on the boundary is known and zero. Land boundaries or boundaries beyond the depth of closure (Hallermeier, 1980) may typically be regarded as closed boundaries.

In general, with one or more free boundaries, sediment may be imported or exported through the boundaries depending on the transportation cost. This may be the case both with and without a bias between predictions and observations. In this respect, our method differs from usual optimal transport methods that do not allow a transport across the boundaries and assume that the total mass is contained within the domain.

We refer to the above algorithm for computing an optimal sediment transport as Effective Transport Difference (ETD), since we resolve a transport field that is fully effective in causing morphodynamic change. An arbitrary transport field, satisfying Eq. (3), can be decomposed into a rotation-free and divergence-free part (Helmholtz decomposition). Only the rotation-free part, which contains the information about the divergence, results in bed-level changes through Eq. (3). Thus, the irrotational, optimal transport field from the least-squares optimization (Eq. (5)) only contains information that can unambiguously be derived from the bed-level differences and boundary conditions.

2.4. Numerical treatment

Section 2.3 presented a partial differential equation approach to obtain the quadratic optimal transport $\mathbf{q}_{L2}$. We have implemented this approach using the functions from the Matlab Partial Differential Equation (PDE) Toolbox, which employs a Finite Element Method (FEM) solver for problems on an unstructured grid (Mathworks, 2015). For now, our implementation has been targeted to relatively simple 2D cases, such as shown in this paper (Sections 3.2 and 4).

The complex geometry, as required by the PDE toolbox, is generated starting with a rectangular domain from which any "dry points", representing, for instance, barrier islands, are excluded (see Section 4). The boundary enclosing the complex geometry, is subdivided into multiple segments, for which a choice between free or closed boundary conditions is available. The Poisson equation is solved on a triangular Delaunay mesh, which is step-wise refined until the solution converges.

3. Simple cases

In this section, we compare the behaviour of the RMSTE and RMSE for simple 1D and 2D cases. First, the 1D cases in Section 3.1 show that the RMSTE does not suffer from the limitations of the RMSE, viz. insensitivity to misplacement distance and the double penalty effect. Next, Section 3.2 confirms these conclusions based on a simple 2D example. Section 3.2 also discusses the characteristics of the 2D optimal transport field and potential for both free and closed boundaries.

3.1. Metric behaviour in 1D

The 1D predictions, h_1, and observations, h_2, are represented by equally wide, Gaussian-shaped humps ($\sigma = 3$) on an otherwise flat bed, with amplitudes and centre points a_1 and x_1 and a_2 and x_2, respectively, such that the misplacement distance is $d = |x_1 - x_2|$ (Fig. 1(a)). Our aim is to compare the behaviour of the RMSTE and RMSE for varying misplacement distance d and amplitude ratio $a_1 a_2^{-1}$. For $x_2 = 0, 10, 20$ and 35 m, x_1 was varied such that the predictions were positioned everywhere in the domain. The observed amplitude a_2 was fixed at 1.33 m, while the amplitude of the predictions a_1 varied as $0 \leqslant a_1 a_2^{-1} \leqslant 2$. When the misplacement distance d is larger than the feature width and $a_1 a_2^{-1} = 0$, the classic double penalty case is obtained.

Obviously, in order to compute the RMSTE, first $q(x)$ needs to be solved. In 1D, if the transport is known at one of the boundaries, for instance $q = 0$, the volume balance has no excess degrees of freedom and only one solution exists, which is found by straightforward numerical integration. This is equivalent to solving the 1D Poisson equation with a closed boundary ($q = 0$) at one end of the domain and an unconstrained boundary ($\phi = 0$) at the other end. Only if the transport is unknown at the boundaries, there is (some) room for optimization in 1D. Considering that the optimal transport q_{L2} is given by the gradient of the potential, the unconstrained condition $\phi = 0$ at either boundary of a 1D domain implies that the transport integrated over the domain is zero, and, thus, the average transport $\overline{q} = 0$. The optimal solution is therefore easily found by integration of the volume balance, while requiring $\overline{q} = 0$. The addition of any nonzero constant to the optimal transport, although still satisfying the volume balance, would increase the transport cost without contributing to bed level changes.

In the presence of a bias, when $\overline{h}_1 \neq \overline{h}_2$, at least one boundary should be free for a solution to exist. For the examples in this section, we have used free boundary conditions at both ends of the domain. Since the

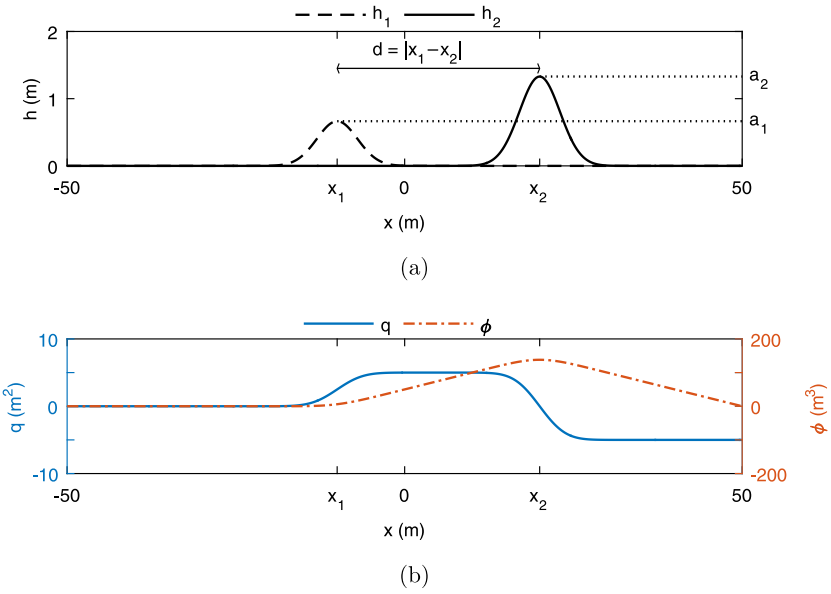

Fig. 1. Lay-out of the 1D cases with an example solution: (a) predicted and observed bathymetries, h_1 and h_2 respectively, consist of equally wide Gaussian shaped humps ($\sigma = 3$) on a flat bed with amplitudes and centre points a_1 and x_1 and a_2 and x_2, respectively and the distance between the two bathymetries $d = |x_1 - x_2|$ (depicted is $a_1 = 0.67$ m, $x_1 = -10$ m, $a_2 = 1.33$ m and $x_2 = 20$ m), (b) the corresponding optimal transport $q(x)$ and potential $\phi(x)$ with $\phi(-50) = \phi(50) = 0$ (free boundaries) and, thus, the domain-averaged transport $\overline{q} = 0$.

free boundary is less constrained than the closed boundary, this will always result in the smallest transport cost.

Fig. 1(b) depicts $\phi(x)$ and $q(x)$ corresponding to h_1 and h_2 as shown in Fig. 1(a). The transports are defined positive in positive x-direction and negative in negative x-direction. The potential $\phi(x)$ is zero at the boundaries and increases with x for positive transports and decreases with x for negative transports, its slope representing the transport magnitude. Obviously, q increases where sediment needs to be eroded and decreases where it needs to be deposited, with the changes in q equal to the volume changes. The average transport $\overline{q} = 0$. The bias requires sediment to be imported, which is, because of the position of the features relative to the boundaries, most cost-efficiently done from the right boundary only, towards the observed feature, such that $q(-50) = 0$. All sediment contained in the excess height $\delta_1 = \max(h_1 - h_2, 0)$ of the predicted, left hump is moved to the right for the benefit of the larger deficit height $\delta_2 = \max(h_2 - h_1, 0)$ of the observed, right hump.

Figs. 2(a) and 2(c) show the RMSE and RMSTE, respectively, as a function of feature misplacement d. Fig. 2(a) illustrates that for two equally sized features ($a_1 = a_2$), the RMSE rapidly increases with increasing d, until, when d is larger than the feature width, the RMSE attains a constant value. This value is a factor $\sqrt{2}$ larger than the RMSE for a flat bed, since the double penalty on the MSE translates to the RMSE as a factor $\sqrt{2}$. In contrast, the RMSTE shows an increase with increasing misplacement distances d, until at relatively large d the proximity of the boundaries forces RMSTE to decrease (Fig. 2(c)); at smaller feature spacings, δ_2 is almost fully replenished by δ_1, whereas at larger feature spacing, it becomes more favourable to also export and import sediment in order to excavate δ_1 and fill δ_2, respectively. Note that for closed boundaries RMSTE is strictly increasing with d (not shown).

For equally sized features, $a_1 = a_2$, we have $q(-50) = q(50)$. As a consequence the RMSTE depends on the misplacement distance d only, regardless of the values of x_1 and x_2. The RMSTE for the flat bed prediction strongly depends on the position of the observed hump relative to the boundary and, hence, on x_2, since the entire deficit height δ_2 must be imported. It follows from Fig. 2(c) that for not too large x_2 and d, the RMSTE is larger for the missed feature than for the misplaced feature.

Fig. 2(b) confirms that the RMSE rewards an underprediction of the feature amplitude. For a feature, misplaced over a distance smaller than its width, RMSE is minimized for values of $0 < a_1 a_2^{-1} \leqslant 1$. For misplacements larger than the feature size, the flat bed prediction, $a_1 = 0$, receives the smallest RMSE. Although the RMSTE also has minima at values of $a_1 < a_2$ for $d > 0$, these minima appear at values of $a_1 a_2^{-1}$ relatively close to 1 (Fig. 2(d)). Note that Figs. 2(b) and 2(d) are valid for $x_2 = 0$.

The above demonstrates that: (1) the RMSTE, as opposed to the RMSE, is able to account for misplacement distance; and (2) that the double penalty effect is specific to the RMSE. Whether or not the RMSTE is larger for a flat bed prediction than for a correctly sized but misplaced feature depends strongly on the situation.

3.2. Demonstration for simple 2D case

In this section, we present a simple example to illustrate the behaviour of the RMSTE in 2D and to provide insight in the characteristics of the 2D potential and optimal transport fields, for various boundary conditions.

Fig. 3 compares an observed 2D feature with three suboptimal predictions: (1) a flat bed prediction, (2) a misplaced feature, and (3) a misplaced feature at a larger misplacement distance. The (R)MSE and RMSTE error values are given in Table 1. The RMSTE is computed with three different sets of boundary conditions: free boundaries only, closed boundaries only (not applicable for a bias) and a combination of a closed South boundary and free boundaries elsewhere (further on referred to as combination boundaries). The different boundary conditions result in the same ranking of the three predictions. However, fewer constraints lead to lower transport costs, such that for all predictions the lowest RMSTE is obtained for free boundaries.

Of course, predictions 2 and 3 are diagnosed with an MSE and RMSE that are larger by a factor 2 and $\sqrt{2}$, respectively, than for prediction 1; prediction 2 and 3 are penalized twice, both where the predicted feature is and where it should be, whereas prediction 1 is penalized at the location of the observed feature only (see Fig. 3). As opposed to the RMSE, the RMSTE distinguishes between prediction 2 and 3, the feature with the smaller misplacement distance (prediction 2) receiving the lower RMSTE. Prediction 2 also outperforms the flat bed prediction

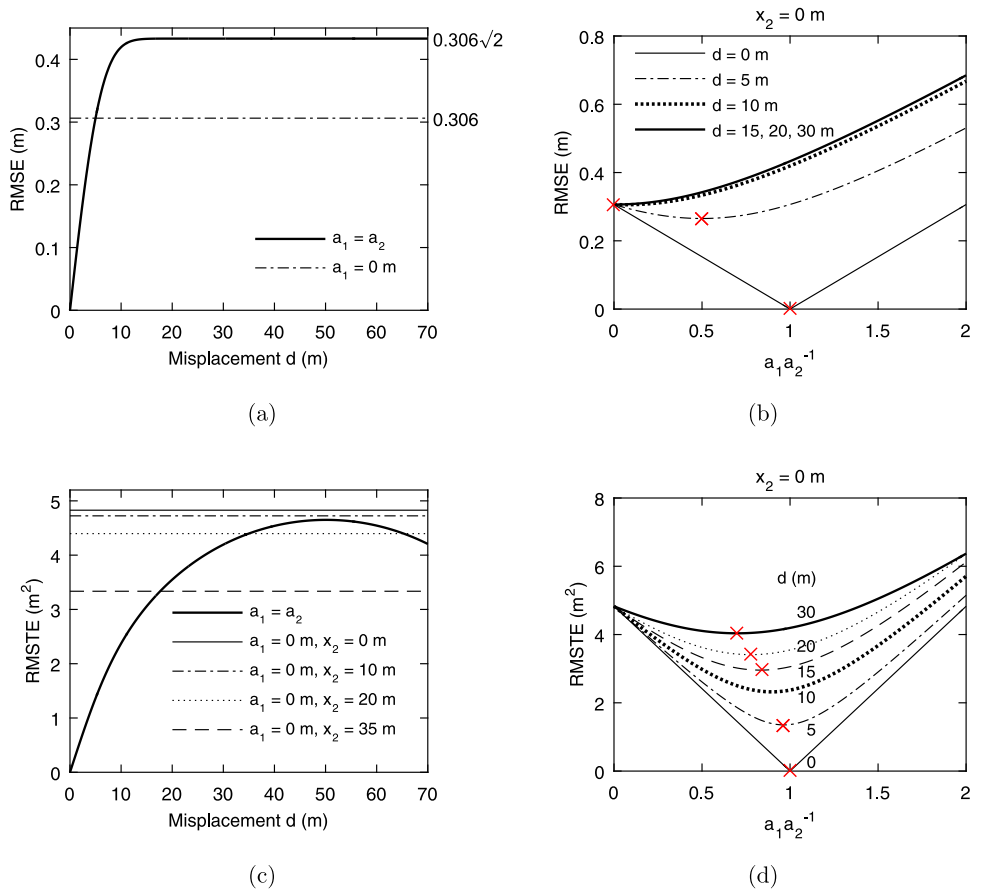

Fig. 2. Behaviour of RMSE and RMSTE, for free boundaries, for the 1D cases introduced in Fig. 1: (a) RMSE as a function of misplacement distance d for predictions with a correct amplitude and for a flat bed prediction, (b) RMSE as a function of amplitude ratio $a_1 a_2^{-1}$ for various misplacement distances d and the centre position of the observations at $x_2 = 0$ m, (c) RMSTE as a function of d for correctly predicted amplitudes as well as for flat bed predictions compared to observations at various centre positions x_2, and (d) RMSTE as a function of $a_1 a_2^{-1}$ for various misplacement distances d and the centre position of the observations at $x_2 = 0$ m. The red crosses in (b) and (d) indicate the minima. (For interpretation of the references to colour in this figure legend, the reader is referred to the web version of this article.)

Table 1
(R)MSE and RMSTE with free, combination (only South boundary closed) and closed boundaries, for predictions 1, 2 and 3.

Prediction	MSE ($\times 10^{-2}$ m^2)	RMSE ($\times 10^{-1}$ m)	$\text{RMSTE}_{\text{free}}$ ($\times 10^{-2}$ m^2)	$\text{RMSTE}_{\text{combination}}$ ($\times 10^{-2}$ m^2)	$\text{RMSTE}_{\text{closed}}$ ($\times 10^{-2}$ m^2)
1	1.05	1.03	1.04	1.08	n.a.
2	2.11	1.45	0.87	0.90	0.94
3	2.11	1.45	1.11	1.23	1.32

(prediction 1), while the feature with the larger misplacement distance (prediction 3) obtains the worst score.

Evidently, in line with the findings for the 1D cases (Section 3.1), for correctly sized features, the RMSTE increases with misplacement distance, until, in the extreme, sediment exchanged across the model boundaries may lead to a lower RMSTE. As discussed in Section 3.1, whether or not a misplaced feature outperforms a missed feature is determined by the (optimal transport cost for) the considered morphological patterns and, hence, depends on the boundary conditions, the size and shape of the observed and misplaced features and their position relative to each other and to the domain boundaries.

Fig. 4 illustrates the characteristics of the potential and optimal transport for prediction 3, using closed boundaries. The left panel shows the optimal transport field moving sediment from the excess height δ_1 to the deficit height δ_2, hence from the red to the blue patches, at minimum cost. The transport field $\mathbf{q} = \nabla\phi$ is fully determined by the potential ϕ (bottom right panel), given by Poisson's Eq. (8). Thus, the transport occurs everywhere at right angles to the equipotential lines, i.e. the lines of constant ϕ, and the spacing of the equipotential lines

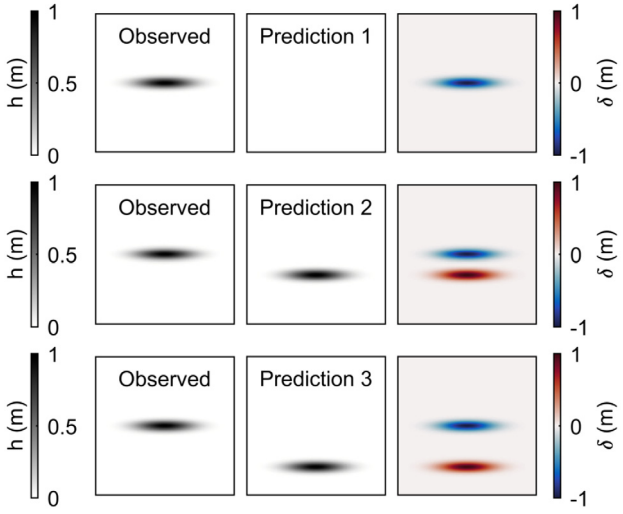

Fig. 3. Three alternative predictions of the same observed feature. Top panels: the featureless prediction 1 has a nonzero difference δ between predicted and observed depth values at the location of the observed feature only. Middle panels: prediction 2, which reproduces the feature at the wrong location, is penalized twice, since δ is nonzero both where the predicted feature is and where it should be. Lower panels: prediction 3, with a larger misplacement distance, is also penalized twice. (For interpretation of the references to colour in this figure legend, the reader is referred to the web version of this article.)

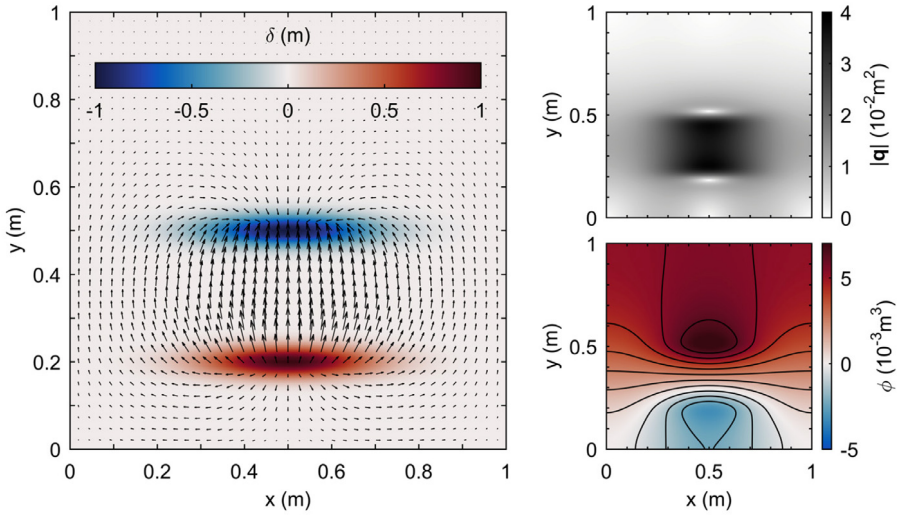

Fig. 4. Optimal solution, with closed boundaries, for prediction 3. *Left panel*: bed level difference $\delta = h_1 - h_2$ with the arrows indicating the transport field (length and direction of arrows indicative of the transport magnitude and direction, respectively). *Right panels*: transport field represented by the transport magnitude (*top*) and potential ϕ (*bottom*). (For interpretation of the references to colour in this figure legend, the reader is referred to the web version of this article.)

reflects the transport magnitude (top right panel), from which RMSTE is easily computed. At the closed boundaries, the equipotential lines are perpendicular to the boundaries, corresponding to zero transport through the boundaries. Naturally, the quadratic cost function governs the transport pattern. The transport magnitudes at different locations are weighted quadratically, so extremes are heavily penalized. This leads to the observed somewhat diffuse transport pattern with curved transport pathways.

Fig. 5 shows the transport magnitude and potential for the situation of free boundaries all around as well as for combination boundaries, which combine a closed South boundary with free boundaries elsewhere. One can verify that the potential is zero at free boundaries allowing transport across the boundaries. The transport magnitudes are smallest when all boundaries are free, resulting in the lowest RMSTE (see Table 1). Unless there is additional knowledge about the error on the boundaries, for instance for a boundary physically closed to sediment, the use of free boundaries is advised (see Section 2.3).

4. Example of a tidal inlet

In this section, we test and illustrate the RMSTE for a more realistic case of a tidal inlet. We diagnose the correspondence between multiple pairs of morphological fields, generated by Delft3D, as well as the relative ranking between the pairs. First, an overview of the model runs and morphological fields is given in Section 4.1. Next, in Section 4.2, we test the behaviour of the RMSTE for fields with misplaced tidal channels due to incorrect Coriolis settings. Subsequently, Section 4.3 presents a full comparison demonstrating the differential behaviour of the RMSE and RMSTE.

4.1. Overview

Starting from an initially highly schematized tidal inlet (Fig. 6), we have generated ten morphological fields with Delft3D. The inlet geometry and boundary forcing are chosen such as to resemble the Wadden Sea inlet of Ameland. The tidal basin is rectangular with an area of 15 × 10 km^2 and a uniform initial depth of 2 m; the entrance has a width of 2 km, and the seabed initially slopes from −2 m at the barrier islands to −10 m at the offshore (Northern) boundary (Roelvink, 2006). The model has a uniform grid size of 100 × 100 m^2.

For the base run O (see Table 2), the latitude was set to 0° and a uniform, harmonic water level variation was applied along the offshore boundary with a period of 12 h and a water level amplitude a of 1 m. The standard sediment transport formulations according to Van Rijn were applied, with a multiplication factor for the suspended sediment reference concentration $f_{sus} = 1$ and a median sediment size $D_{50} = 200$ μm. The other 9 runs listed in Table 2 are variations to the base run O with respect to latitude, f_{sus}, D_{50}, tidal amplitude a and tidal direction. The latter was changed, for run A only, from cross-shore to alongshore by applying a phase difference along the Northern boundary. The final bathymetries of the 10 runs are shown in Fig. 7. For the computation of the ETD and, subsequently, the RMSTE between pairs of depth fields (Sections 4.2 and 4.3), we have considered the land boundaries and sea boundaries as closed and free boundaries, respectively (see Fig. 6).

Table 2
Overview of the 10 runs used to generate the morphological fields of Fig. 7. O is the base run, the others are variations with respect to latitude, tidal amplitude and direction [C(ross)- or L(ongshore)], transport parameter f_{sus} and D_{50}. The labels are chosen such as to be consistent with Bosboom and Reniers (2014b) and Mol et al. (2015).

Run	Latitude	Amplitude (m)	Direction	f_{sus}	D_{50} (μm)
O	0°	1.0	C	1.0	200
A	0°	1.0	L	1.0	200
B	0°	0.67	C	1.0	200
C	0°	1.5	C	1.0	200
D	0°	0.5	C	1.0	200
F	90° N	1.0	C	1.0	200
G	90° S	1.0	C	1.0	200
L	53° N	1.0	C	1.0	200
M	53° N	1.0	C	1.5	200
N	0°	1.0	C	1.0	250

4.2. Variation in coriolis

First, in this section, the model-generated depth fields O, F, G and L (see Table 2 and Fig. 7) are considered, which only differ with respect to the latitude, and, hence, Coriolis parameter. We label depth field L, the one with 53° N, as the observations and regard the other three as three competing predictions. The pairs of computations and observations are named by the label of the predictions followed by the label of the "observations" (see Table 3).

Figs. 8 and 9 show the bed level differences $\delta = h_1 - h_2$ and transport magnitudes $|\mathbf{q}|$, respectively. The required transport corrections are mostly confined to the flood and ebb tidal delta areas, with zero or small transports outside these delta regions. Sediment is relocated from

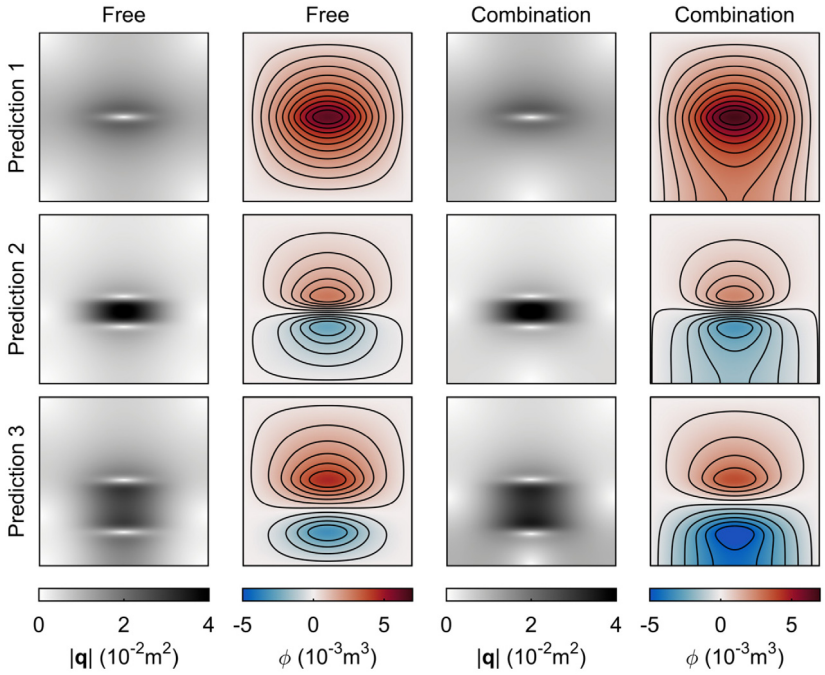

Fig. 5. Transport magnitudes and potential for predictions 1, 2 and 3 for free boundary conditions and combination (South boundary closed, remainder free) boundary conditions. (For interpretation of the references to colour in this figure legend, the reader is referred to the web version of this article.)

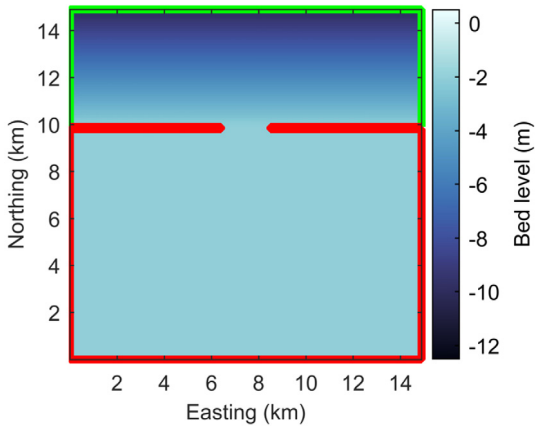

Fig. 6. Initial bathymetry with the free sea boundaries for Poisson's Eq. (8) in green and the closed land boundaries in red. (For interpretation of the references to colour in this figure legend, the reader is referred to the web version of this article.)

the excess locations to the shortage locations, i.e. from the red to the blue patches in Fig. 8. On the ebb tidal delta, this results in a transport between the delta flat and the outer edges in both directions. In the flood tidal delta, sediment is transported to locations where channels are wrongly predicted and away from locations where they should have been predicted. The transport distances are limited, since the Coriolis errors require only local corrections to feature locations.

Both the RMSE and RMSTE increase with increasing latitude deviation (Table 3), since both the misplaced volumes of sediment and the misplacement distances increase with latitude error. Under these circumstances, the various error metrics, including the metrics based on the field deformation or image warping method (see Bosboom and Reniers, 2014b), demonstrate the same qualitative behaviour.

4.3. Comparison of all fields

In this section, the predictions A to N are compared to the observations O by means of the RMSE and the RMSTE (see Table 4).

Table 3
RMSE and RMSTE for three cases with errors in latitude and hence Coriolis parameter. Case names consist of the label of the predictions followed by the label of the "observations", which are taken as the model outcome at 53° N.

Case	Latitude model	Latitude observed	RMSE (m)	RMSTE ($\times 10^2$ m^2)
FL	90° N	53° N	0.29	0.5
OL	0°	53° N	0.52	1.2
GL	90° S	53° N	0.73	2.0

Table 4
RMSE and RMSTE for predictions A to N compared to "observations" O, the model outcome at 0°, hence without the influence of Coriolis.

Case	RMSE (m)	RMSTE ($\times 10^2$ m^2)
AO	0.78	2.6
BO	0.77	5.5
CO	1.16	8.2
DO	0.95[a]	7.8
FO	0.59	1.4
GO	0.59	1.4
LO	0.52	1.2
MO	0.59	2.2
NO	0.47	1.8

[a]Corrected from 0.96 as previously listed in Bosboom and Reniers (2014b).

From Table 4, it is clear that the RMSE and RMSTE lead to a different ranking amongst the predictions, with prediction L receiving the lowest RMSTE and prediction N the lowest RMSE. Further, as opposed to the RMSE, the RMSTE is seen to discriminate between predictions F (or its mirrored prediction G) and M as well as between A and B. The distinctive behaviour of the two error metrics is a logical consequence of their different definition. Below, we highlight and explain some of these differences on the basis of the underlying fields of bed level differences and transports (Figs. 10 and 11).

Prediction L, which has a modelled latitude of 53° N rather than the "real" 0°, is awarded the lowest RMSTE. Predictions F and G,

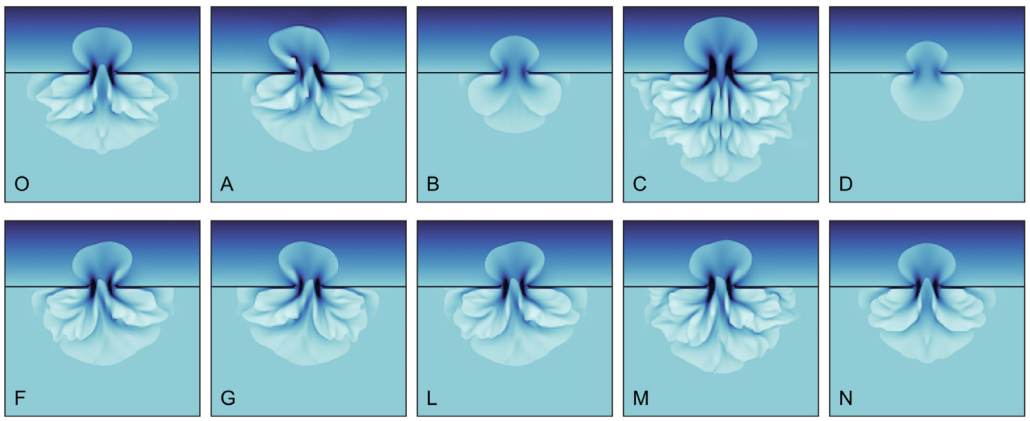

Fig. 7. Final bathymetries of the 10 runs with settings according to Table 2. The horizontal and vertical axes and the colour scaling are as in Fig. 6.

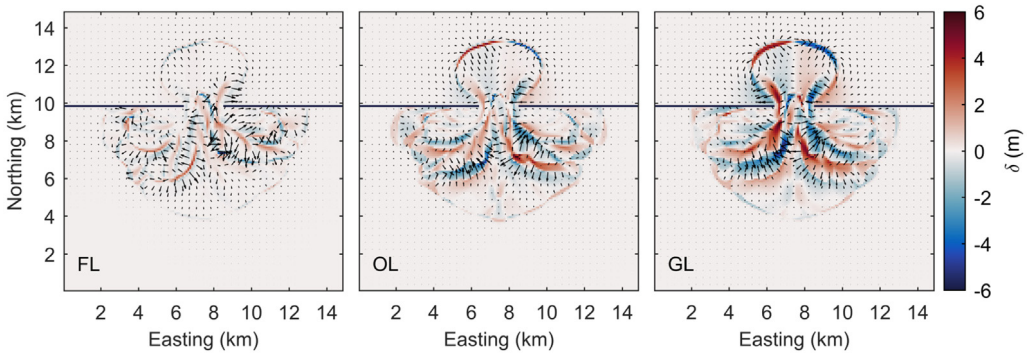

Fig. 8. Bed level differences and transport fields, with the length and direction of the arrows indicative of the transport magnitude and direction, respectively, for cases FL, OL and GL (see Table 3). (For interpretation of the references to colour in this figure legend, the reader is referred to the web version of this article.)

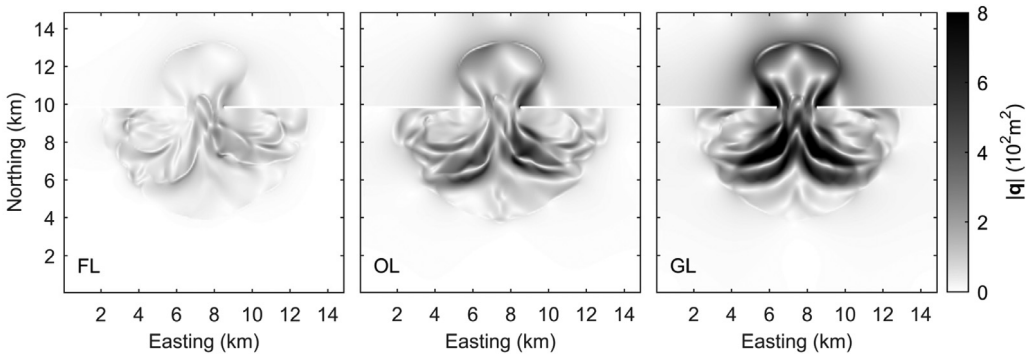

Fig. 9. Transport magnitudes for cases FL, OL and GL with closed land boundaries and free sea boundaries.

with a 90° modelled latitude, receive the second best RMSTE. The wrongly predicted Coriolis deflection leads to a distortion of the outer edges of the ebb tidal delta and a mispositioning of the channels on the flood tidal delta and in the inlet gorge. The sediment transport required to correct these Coriolis errors takes place over short distances only, explaining that, measured by the RMSTE, predictions F, G and L outperform the other predictions, including prediction N, which is the best prediction in terms of RMSE. The too high grain size of the latter prediction results in an underdeveloped delta, which must be corrected by transporting sediment from the channel locations to build the flats and extend the delta rims. The relatively large distances over which this sediment is transported explains the larger RMSTE compared to the predictions with Coriolis error, even though, based on the RMSE, the amount of misplaced sediment is smaller. This underlines again that the RMSE measures misplaced sediment volumes only, whereas the RMSTE takes misplacement distance into account as well.

Despite receiving the same values of RMSE, predictions F and M behave differently in terms of RMSTE. The erroneous Coriolis deflection that both predictions suffer from, is stronger for prediction F than for prediction M. Prediction M, however, has an additional error source that requires a corrective transport over larger distances; due to too large suspended sediment transports (f_{sus} = 1.5 instead of 1), the inlet system is overdeveloped. The corrective transport pattern for prediction M shows the two error sources operating at different spatial scales, of which the longer scales weight heavier towards the RMSTE. The result is a domain-averaged corrective sediment transport that is larger for prediction M than for F.

Predictions A to D were added to allow a comparison with the $RMSE_w$, the combined error metric based on the field deformation or image warping method of Bosboom and Reniers (2014b). The $RMSE_w$ combines all relevant information on location errors and pre- and post-warp intensity (i.e. bed level) errors. It depends on a user-defined

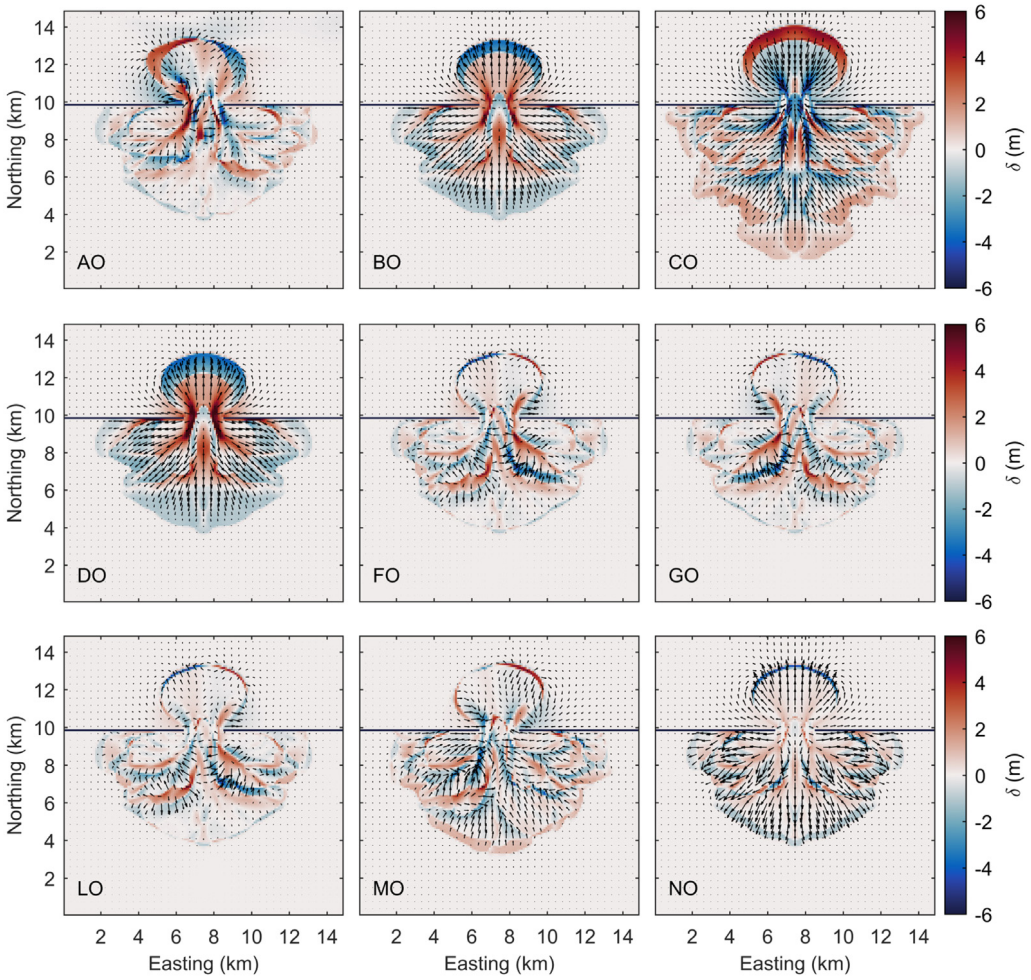

Fig. 10. Bed level differences and transport fields, with the length and direction of the arrows indicative of the transport magnitude and direction, respectively, for predictions A through N compared to the "observations" O. (For interpretation of the references to colour in this figure legend, the reader is referred to the web version of this article.)

Table 5
The combined error metric $RMSE_w$ from the image warp (with D_{max} = 3000 m and 1000 m) for predictions A to D compared to "observations" O (values from Bosboom and Reniers, 2014b). The values for RMSE and RMSTE are copied from Table 4 for ease of reference.

Case	$RMSE_w$ (m) D_{max} = 3000 m	$RMSE_w$ (m) D_{max} = 1000 m	RMSE (m)	RMSTE ($\times 10^2$ m^2)
AO	0.49	0.63	0.78	2.6
BO	0.60	0.71	0.77	5.5
CO	0.78	1.02	1.16	8.2
DO	0.84	0.94	0.95	7.8

parameter D_{max}, which represents the maximum distance over which morphological features may be displaced for the prediction to still get (some) credit for predicting these features. Both the RMSTE and the $RMSE_w$ diagnose prediction A to be a better prediction than B, in spite of the similar values for RMSE (Tables 4 and 5). Whether prediction C or D is diagnosed the better prediction by the $RMSE_w$ depends on the chosen value for D_{max}. In contrast, the RMSTE does not allow such a parameter. Based on the RMSTE, and hence on the required amount of corrective sediment transport, prediction D outperforms prediction C.

A final remark concerns the free boundary conditions. From Figs. 10 and 11, it can be seen that for predictions A to D, with larger morphological change closer to the North boundary, there is a small corrective sediment transport across this boundary. Note that these predictions require a net sediment exchange with the outside world due to the presence of a (small) bias. The contribution of the transport across the North boundary to the RMSTE is limited, as can be verified from Fig. 11.

5. Discussion

Sections 3 and 4 have shown that the newly introduced RMSTE is capable of discriminating among model results, which is an important requirement of any error metric. We have seen that the RMSTE may lead to a different judgement as to which of two predictions is better than the RMSE, since it highlights other aspects of model performance. The RMSE measures the amount of misplaced sediment, and, hence, penalizes small misplacements of features heavily. As a consequence, it is difficult to demonstrate the quality of a high-variability prediction with the RMSE. The RMSTE on the contrary, is based on the corrective sediment transport from the predicted to the observed morphological field and, consequently, not only takes the amount of misplaced sediment into account, but also the distance over which this sediment is misplaced. Hence, larger spatial scales in the bathymetric error fields, requiring larger corrective transport distances, are penalized heavier than shorter scales. For the simple cases in Section 3, this was reflected in the RMSTE increasing with the misplacement distance of the considered features and being free from the consistent favouring of flat bed predictions that the RMSE suffers from. Similarly, Section 4 demonstrated, for more realistic bathymetric patterns, that more localized sediment misplacements, due to, for instance, incorrect Coriolis deflections, are diagnosed with better RMSTE scores than misplacements similar in volume but over larger distances. Section 4 further indicates

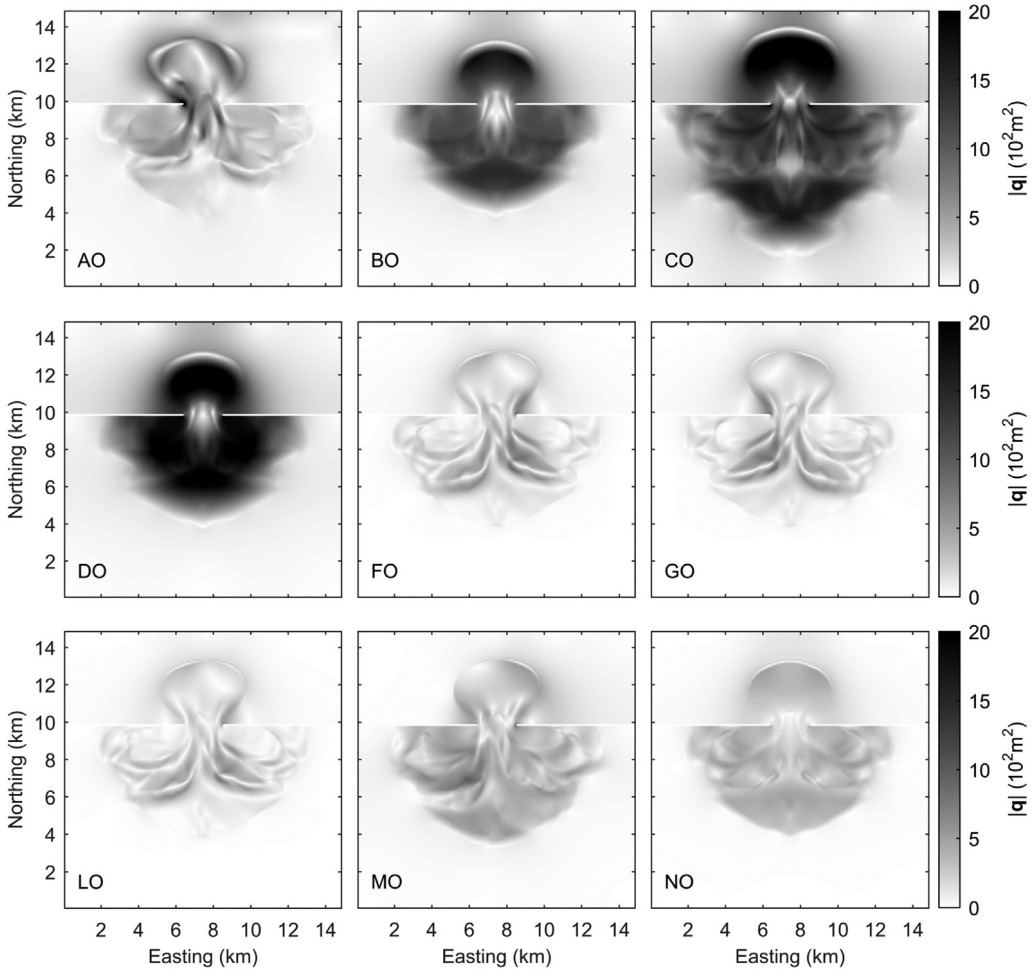

Fig. 11. Transport magnitudes for predictions A through N compared to the "observations" O.

that inspection of the corrective transport fields, underlying the RMSTE, may provide some guidance as to how the model should be improved. As an example, for case MO in Section 4.3, the transport pattern revealed two error sources operating on different spatial scales, which, when isolated, may be separately addressed for the improvement of the model.

Based on the above described results, we expect that the RMSTE will enable a more balanced comparison between morphodynamic model predictions. The current validation practice of only using a point-wise accuracy metric – for example the (R)MSE – or a skill score based on such a point-wise metric – for example the mean-squared-error skill score known as BSS – tends to reward predictions that underestimate the variability of morphodynamic change (Bosboom et al., 2014; Bosboom and Reniers, 2018). This undesirable effect can be counteracted by also taking the RMSTE into account. We further anticipate that the RMSTE will be helpful in calibrating morphodynamic models with respect to the morphodynamic time-scale. In a first calibration step, an automated calibration routine, which minimizes the RMSTE, may be able to determine the optimal global model settings, such as certain transport parameters, that merely affect the morphodynamic time-scale. In a next step, a more detailed calibration of other parameters can be undertaken using multiple error metrics, amongst others the RMSE and the RMSTE.

In Section 3.1, we have seen that the proximity of the boundaries may restrict the increase of the RMSTE with the misplacement distance between two features, or even cause the RMSTE to decrease. This can occur when it is cheaper to (partly) export the excess height δ_1 through the one boundary and (partly) import the deficit height δ_2 through another boundary than to directly move δ_1 towards δ_2. It may seem counterintuitive at first, that free boundaries could prevent a predicted and observed feature on either side of the model domain to be (fully) associated with each other. However, the transport error on the boundary is equally unknown as within the domain, such that free boundaries, which are themselves part of the optimization, are generally the logical choice. Only in the special case of a boundary that is physically closed for sediment, such as land boundaries, one may assume that the transport error on the boundary is known and zero. The transport across free boundaries will be relatively small when the bias between predictions and observations is small and the model boundaries are chosen far away from the regions of morphodynamic change, as would generally be the case in practical applications (see also Section 4). In these cases, also the effect of the boundary conditions on the RMSTE will be small.

As opposed to the RMSE, the RMSTE requires fields to operate on, which complicates its application in data-poor environments. A solution could be to interpolate the data to the computational grid using straightforward interpolation methods. Alternatively, more advanced stochastic models may be used to generate realistic realizations of the seabed, consistent with the available data (Novaczek et al., 2019; Williams et al., 2017). The sensitivity of the RMSTE to data coverage and resolution can be assessed in practice by evaluating the difference between the RMSTE values computed using different methods to estimate missing data. Note that both the RMSE and the RMSTE can be expected to be sensitive to the spatial resolution of the data. In fact, the sensitivity of the RMSTE to spatial resolution is likely to be smaller than of the RMSE, since the first gives more weight to larger spatial

scales in the bathymetric error fields than to shorter scales. This also raises the question of the validity of computing the RMSE based on the measurement locations only, which could also be addressed by a sensitivity analysis using multiple realizations of the seabed consistent with the measurements.

In principle, a skill score could readily be derived from the RMSTE, in the same manner as skill scores have been derived from the (R)MSE (Gallagher et al., 1998; Sutherland et al., 2004). Like any skill score, it would inherit the characteristics of the error metric it is based on, in this case the RMSTE, and be critically dependent on the choice of the reference prediction. We expect however that the common choice of the initial morphology as the reference prediction will not be able to create the required level playing field, as was previously demonstrated for the MSESS/BSS (Bosboom et al., 2014; Bosboom and Reniers, 2018).

The ETD expresses the mismatch between predictions and observations in terms of a sediment transport field that is able to transform the predictions to perfectly match the observations. This method, by definition, allows for the redistribution of the excess sediment volume though splitting or coalescing and implies that bed features are not necessarily kept intact. While bed forms are created or flattened out, sediment is redistributed over the morphological scales. The transport direction of sediment contained in a misplaced feature is not necessarily the same as the direction in which the predicted feature needs to be moved. In the examples of Section 3, the direction of feature movement, for instance from left to right, coincided with the transport direction of the sediment contained in the predicted feature. If we would multiply the bed levels by -1, such that the features were channels rather than humps, the required feature displacement would still be from left to right, but the sediment, rather, would be moved towards the predicted feature, from right to left; the excess height δ_1 and deficit height δ_2 are now found at the location of the observations and predictions, respectively, instead of the other way around. This highlights one of the important differences between the ETD, which moves sediment, and the image warp, such as employed in Bosboom and Reniers (2014b), which, roughly speaking, moves features. This warping method finds an optimal displacement field by minimizing a regular L^2 distance (Eq. (1), with $p = 2$). It essentially shifts pixels by (locally) stretching or compressing the morphological pattern to better match the observations. Bed level differences between corresponding features in the predictions and observations prevent an exact match. The combined error metric $\mathrm{RMSE_w}$ as presented in Bosboom and Reniers (2014b) weights both the remaining RMSE after the optimal transformation and the magnitude of the displacements required to obtain this reduced error, according to a user-defined parameter. As a consequence, the $\mathrm{RMSE_w}$ can be expected to capture the visual disagreement between morphological patterns, whereas the RMSTE represents the minimum cost, in terms of (squared) sediment transport and, hence, work, to bridge the deviations between the morphological patterns. Advantages of the ETD method over the image warp are that the ETD is mass-conserving, parameter-free and symmetric, the optimal transport from observations to predictions being the inverse of the optimal transport from predictions to observations.

The transport fields $\mathbf{q}_{L2}$, as found in Sections 3 and 4, are cumulative, corrective and net transport fields. Here, *cumulative* refers to the time-integration of the transport and *corrective* signifies that the transport fields represent the transport differences between predictions and observations, rather than observed or modelled transports between consecutive moments in time. Further, *net* expresses that they present the "cheapest" way, based on the 2-norm of the transport field, to move the mispredicted sediment volumes to the right locations. Thus, from the multitude of corrective transport fields satisfying the volume balance Eq. (3), the transport that minimizes the amount of squared work is thought to best represent the mismatch between predictions and observations. Since the optimal transport $\mathbf{q}_{L2}$ is irrotational, it is fully effective in causing morphodynamic change and only contains information that can unambiguously be derived from the bed-level differences and boundary conditions, see Section 2.3. The physical justification of $\mathbf{q}_{L2}$ as the optimal transport is found in the choice of the cost function formulated in terms of work, rather than in a connection to the usual transport descriptions based on hydrodynamic drivers, which may lead to transport fields that are not optimized with respect to the cost function. Obviously, the exponent p in the cost function can be expected to influence the transport pattern. With our pragmatic choice of $p = 2$, the transport magnitudes at different locations are weighted quadratically, so extremes are heavily penalized. This leads to somewhat smeared out transport patterns with curved transport pathways, as found in Sections 3 and 4. With $p = 1$ on the other hand, the transport magnitudes at different locations are weighted proportionally, so the cost function is likely to be less affected by local large transports, which may lead to more pronounced transport patterns.

6. Conclusions and perspectives

In this paper, we have presented a novel diagnostic tool for morphodynamic model validation. The employed ETD method solves an optimal transport problem that moves sediment from the one bathymetry (the predictions) to the other bathymetry (the observations) at minimum quadratic transport cost and, thus, work. The quadratic cost function allows a reformulation of the problem in terms of a Poisson partial differential equation, which is uniquely solvable, at least up to an additive constant. A new error metric, the RMSTE, is defined as a constant multiple of the optimal quadratic cost. As such, it measures the error in terms of the net corrective sediment transport volume required for a match with the observations. By penalizing the total sediment transport, the spatial structure of the error is taken into account; the RMSTE is sensitive to the volumes of misplaced sediment as well as to the distance over which this sediment must be transported. Advantages of the ETD method over the image warp of Bosboom and Reniers (2014b) are that the ETD is mass-conserving, parameter-free and symmetric, the optimal transport from observations to predictions being the inverse of the optimal transport from predictions to observations.

The results have shown that the RMSTE, as opposed to the RMSE, is able to discriminate between predictions that differ in the misplacement distance of predicted morphological features. Also, the RMSTE avoids the consistent favouring of the underprediction of the variability of morphodynamic change that point-wise accuracy metrics, such as the RMSE, and the mean-squared-error skill score known as BSS are prone to.

By definition, each error metric condenses a large amount of data into a single number, therewith highlighting certain aspects of morphological model performance only. Therefore, we recommend that a combination of metrics is used in the validation of morphological models and that the weighting is determined by the goal of the simulation. We expect that the addition of the RMSTE enables a fairer comparison between morphodynamic model predictions, by avoiding some of the pitfalls of point-wise metrics and by defining the error in terms of a quantity that is at the heart of morphodynamic model validation.

In future studies, the behaviour of the RMSTE in a range of practical applications will need to be considered. In order to do so, a more robust implementation of the ETD is required in order to deal with arbitrary model domains. Further, we anticipate that valuable additional information can be extracted from the optimal transport fields by isolating the various scales in the transport fields, for instance using our scale-selective validation method (Bosboom and Reniers, 2014a).

The choice of $p = 2$ in the optimization problem, leading to quadratic transport costs, has enabled a relatively straightforward solution procedure resulting in a rotation-free optimal transport. For $p = 1$ and a domain boundary closed to sediment, our formulation and the L^p Monge–Kantorovich problem are equivalent and correspond to the original Monge mass transfer, which guarantees the shortest possible weighted transport distance and smallest transport magnitude.

Numerical methods for solving the L^1 problem exist (Benamou and Carlier, 2015), but are considerably more complex than our L^2 solution procedure. Nonetheless, it may be worthwhile to explore possibilities to solve the L^1 optimization problem. Such an approach would lead to the introduction of a new error metric, the mean absolute transport error (MATE), which can be expected to behave differently than the RMSTE. The MATE is to the RMSTE as the MAE is to RMSE, with that difference that MATE is based on $\mathbf{q}_{L1}$ rather than $\mathbf{q}_{L2}$.

Declaration of competing interest

The authors declare that they have no known competing financial interests or personal relationships that could have appeared to influence the work reported in this paper.

CRediT authorship contribution statement

J. Bosboom: Conceptualization, Methodology, Validation, Formal analysis, Investigation, Writing - original draft, Writing - review & editing, Visualization. **M. Mol:** Software, Validation, Formal analysis, Investigation. **A.J.H.M. Reniers:** Conceptualization, Writing - review & editing. **M.J.F. Stive:** Writing - review & editing. **C.F. de Valk:** Conceptualization, Methodology, Writing - review & editing.

Acknowledgements

We thank the reviewers for their constructive comments, which resulted in an improved paper.

Appendix. Proof of irrotationality of transport field

Here we prove the claim in Section 2.3 that the minimizer of

$$\left| \int_{\mathbf{x}\in\Omega} |\mathbf{q}(\mathbf{x})|^2 \, \mathrm{d}\mathbf{x} \right|^{1/2} \tag{A.1}$$

under the constraint of the volume balance (Eq. (3)) is irrotational. The corresponding Lagrangian $\mathcal{L}$ is

$$\mathcal{L}(\mathbf{q}, \lambda) := \int_{\mathbf{x}\in\Omega} \frac{1}{2} |\mathbf{q}(\mathbf{x})|^2 \, \mathrm{d}\mathbf{x} + \int_{\mathbf{x}\in\Omega} \lambda(\mathbf{x}) \left(\nabla \cdot \mathbf{q}(\mathbf{x}) + h_2(\mathbf{x}) - h_1(\mathbf{x})\right) \tag{A.2}$$

with λ the Lagrange multiplier for the constraint and $\nabla\cdot$ the divergence operator. Note that the first term is equivalent to Eq. (A.1) as the cost function. At the minimum, the variation of the Lagrangian ($\delta\mathcal{L}$) with respect to $\mathbf{q}$ is zero, hence:

$$0 = \delta\mathcal{L}(\mathbf{q}, \lambda) = \int_{\mathbf{x}\in\Omega} \left(\mathbf{q}(\mathbf{x}) \cdot \delta\mathbf{q}(\mathbf{x}) + \lambda(\mathbf{x}) \, \nabla \cdot \delta\mathbf{q}(\mathbf{x})\right) \mathrm{d}\mathbf{x} \tag{A.3}$$

with $\cdot$ denoting the inner product. Using partial integration, Eq. (A.3) can be rewritten as:

$$0 = \int_{\mathbf{x}\in\Omega} \left(\mathbf{q}(\mathbf{x}) - \nabla\lambda(\mathbf{x})\right) \cdot \delta\mathbf{q}(\mathbf{x}) \mathrm{d}\mathbf{x} - \int_{\mathbf{x}\in\partial\Omega} \lambda(\mathbf{x}) (\delta\mathbf{q}(\mathbf{x}) \cdot \mathbf{n}(\mathbf{x})) \mathrm{d}\mathbf{x} \tag{A.4}$$

with $\mathbf{n}$ the inward normal to the boundary $\partial\Omega$ of Ω.

Typically, we either have that $\mathbf{q}\cdot\mathbf{n}$ on the boundary $\partial\Omega$ is known, and, thus, $\delta\mathbf{q}\cdot\mathbf{n} = 0$ on $\partial\Omega$ or that $\mathbf{q}\cdot\mathbf{n}$ on the boundary $\partial\Omega$ is unknown, which, because there is no constraint on $\mathbf{q}$ on the boundary, translates to $\lambda = 0$ on $\partial\Omega$. The latter, unconstrained boundary condition is referred to as free boundary in this paper, whereas the first, specified boundary condition has the employed closed boundary as a special example. With either $\delta\mathbf{q}\cdot\mathbf{n} = 0$ or $\lambda = 0$ on $\partial\Omega$, the last term of Eq. (A.4) equals zero, and Eq. (A.4) implies, since $\delta\mathbf{q}$ is arbitrary in the interior of Ω, $\mathbf{q}(\mathbf{x}) = \nabla\lambda(\mathbf{x})$. Therefore, we have

$$\mathbf{q}(\mathbf{x}) = \nabla\phi(\mathbf{x}) \tag{A.5}$$

with $\phi = \lambda$ satisfying Eq. (8) in the interior of Ω and either $\nabla\phi\cdot\mathbf{n} = 0$ or $\phi = 0$ on $\partial\Omega$.

This proves that the 2-norm of $\mathbf{q}$ is minimal if the vector field $\mathbf{q}$ is irrotational.

References

Anthes, R.A., 1983. Regional models of the atmosphere in middle latitudes. Mon. Weather Rev. 111 (6), 1306–1335. http://dx.doi.org/10.1175/1520-0493(1983)111<1306:RMOTAI>2.0.CO;2.

Arpe, K., Hollingsworth, A., Tracton, M.S., Lorenc, A.C., Uppala, S., Kållberg, P., 1985. The response of numerical weather prediction systems to FGGE level IIb data. Part II: Forecast verifications and implications for predictability. Q. J. R. Meteorol. Soc. 111 (467), 67–101. http://dx.doi.org/10.1002/qj.49711146703.

Benamou, J.-D., Brenier, Y., 2000. A computational fluid mechanics solution to the Monge–Kantorovich mass transfer problem. Numer. Math. 84 (3), 375–393. http://dx.doi.org/10.1007/s002110050002.

Benamou, J.-D., Brenier, Y., Guittet, K., 2002. The Monge–Kantorovitch mass transfer and its computational fluid mechanics formulation. Int. J. Numer. Methods Fluids 40 (1–2), 21–30. http://dx.doi.org/10.1002/fld.264.

Benamou, J.-D., Carlier, G., 2015. Augmented Lagrangian methods for transport optimization, mean field games and degenerate elliptic equations. J. Optim. Theory Appl. 167 (1), 1–26. http://dx.doi.org/10.1007/s10957-015-0725-9.

Bogachev, V.I., Kolesnikov, A.V., 2012. The Monge–Kantorovich problem: achievements, connections, and perspectives. Russian Math. Surveys 67 (5), 785–890. http://dx.doi.org/10.1070/RM2012v067n05ABEH004808.

Bosboom, J., Reniers, A., 2014a. Scale-selective validation of morphodynamic models. In: Proceedings 34th International Conference on Coastal Engineering, Vol. 3. Seoul, South-Korea, pp. 1911–1920. http://dx.doi.org/10.9753/icce.v34.sediment.75.

Bosboom, J., Reniers, A.J.H.M., 2014b. Displacement-based error metrics for morphodynamic models. Adv. Geosci. 39, 37–43. http://dx.doi.org/10.5194/adgeo-39-37-2014.

Bosboom, J., Reniers, A., 2018. The deceptive simplicity of the Brier skill score. In: Kim, Y.C. (Ed.), Handbook of Coastal and Ocean Engineering. pp. 1639–1663. http://dx.doi.org/10.1142/9789813204027_0058.

Bosboom, J., Reniers, A.J.H.M., Luijendijk, A.P., 2014. On the perception of morphodynamic model skill. Coast. Eng. 94, 112–125. http://dx.doi.org/10.1016/j.coastaleng.2014.08.008.

Bougeault, P., 2003. The WGNE Survey of Verification Methods for Numerical Prediction of Weather Elements and Severe Weather Events. CAS/JSC WGNE Report, 18, WMO/TD-NO. 1173 Appendix C, pp. 1–11, URL http://www.wcrp-climate.org/documents/wgne18rpt.pdf.

Brenier, Y., 2003. Extended Monge–Kantorovich theory. In: Optimal Transportation and Applications. Springer Berlin Heidelberg, pp. 91–121. http://dx.doi.org/10.1007/978-3-540-44857-0_4.

Dam, G., van der Wegen, M., Labeur, R.J., Roelvink, D., 2016. Modeling centuries of estuarine morphodynamics in the Western Scheldt estuary. Geophys. Res. Lett. 43 (8), 3839–3847. http://dx.doi.org/10.1002/2015GL066725.

Davidson, M.A., Splinter, K.D., Turner, I.L., 2013. A simple equilibrium model for predicting shoreline change. Coast. Eng. 73, 191–202. http://dx.doi.org/10.1016/j.coastaleng.2012.11.002.

Dodet, G., Castelle, B., Masselink, G., Scott, T., Davidson, M., Floc'h, F., Jackson, D., Suanez, S., 2019. Beach recovery from extreme storm activity during the 2013–14 winter along the Atlantic coast of Europe. Earth Surf. Process. Landf. 44 (1), 393–401. http://dx.doi.org/10.1002/esp.4500.

Elmilady, H., van der Wegen, M., Roelvink, D., Jaffe, B.E., 2019. Intertidal area disappears under sea level rise: 250 years of morphodynamic modeling in San Pablo bay, California. J. Geophys. Res. Earth Surf. 124 (1), 38–59. http://dx.doi.org/10.1029/2018JF004857.

Evans, L.C., 1997. Partial differential equations and Monge–Kantorovich mass transfer. In: Current Developments in Mathematics. (1), International Press of Boston, pp. 65–126, URL https://math.berkeley.edu/~evans/Monge-Kantorovich.survey.pdf.

Fortunato, A.B., Nahon, A., Dodet, G., Pires, A.R., Freitas, M.C., Bruneau, N., Azevedo, A., Bertin, X., Benevides, P., Andrade, C., Oliveira, A., 2014. Morphological evolution of an ephemeral tidal inlet from opening to closure: The Albufeira inlet, Portugal. Cont. Shelf Res. 73, 49–63. http://dx.doi.org/10.1016/j.csr.2013.11.005.

Gallagher, E.L., Elgar, S., Guza, R., 1998. Observations of sand bar evolution on a natural beach. J. Geophys. Res. Oceans (1978–2012) 103 (C2), 3203–3215. http://dx.doi.org/10.1029/97JC02765.

Ganju, N.K., Jaffe, B.E., Schoellhamer, D.H., 2011. Discontinuous hindcast simulations of estuarine bathymetric change: A case study from Suisun Bay, California. Estuar. Coast. Shelf Sci. 93 (2), 142–150. http://dx.doi.org/10.1016/j.ecss.2011.04.004.

Gilleland, E., Ahijevych, D., Brown, B.G., Casati, B., Ebert, E.E., 2009. Intercomparison of spatial forecast verification methods. Weather Forecast. 24 (5), 1416–1430. http://dx.doi.org/10.1175/2009WAF2222269.1.

Hallermeier, R.J., 1980. A profile zonation for seasonal sand beaches from wave climate. Coast. Eng. 4, 253–277. http://dx.doi.org/10.1016/0378-3839(80)90022-8.

Hallin, C., Huisman, B.J., Larson, M., Walstra, D.-J.R., Hanson, H., 2019. Impact of sediment supply on decadal-scale dune evolution — Analysis and modelling of the Kennemer dunes in the Netherlands. Geomorphology 337, 94–110. http://dx.doi.org/10.1016/j.geomorph.2019.04.003.

Henderson, S.M., Allen, J.S., Newberger, P.A., 2004. Nearshore sandbar migration predicted by an eddy-diffusive boundary layer model. J. Geophys. Res. Oceans 109 (C6), C06024. http://dx.doi.org/10.1029/2003JC002137.

Luijendijk, A.P., Ranasinghe, R., de Schipper, M.A., Huisman, B.A., Swinkels, C.M., Walstra, D.J.R., Stive, M.J.F., 2017. The initial morphological response of the Sand Engine: a process based modelling study. Coast. Eng. 119, 1–14. http://dx.doi.org/10.1016/j.coastaleng.2016.09.005.

Luijendijk, A.P., de Schipper, M.A., Ranasinghe, R., 2019. Morphodynamic acceleration techniques for multi-timescale predictions of complex sandy interventions. J. Mar. Sci. Eng. 7 (3), http://dx.doi.org/10.3390/jmse7030078.

Mathworks, 2015. MATLAB and Partial Differential Equation Toolbox Release 2015b. The MathWorks, Inc., Natick, Massachusetts, United States.

McCall, R.T., Masselink, G., Poate, T.G., Roelvink, J.A., Almeida, L.P., 2015. Modelling the morphodynamics of gravel beaches during storms with XBeach-G. Coast. Eng. 103, 52–66. http://dx.doi.org/10.1016/j.coastaleng.2015.06.002.

McCall, R.T., van Thiel de Vries, J.S.M., Plant, N.G., van Dongeren, A.R., Roelvink, J.A., Thompson, D.M., Reniers, A.J.H.M., 2010. Two-dimensional time dependent hurricane overwash and erosion modeling at Santa Rosa Island. Coast. Eng. 57 (7), 668–683. http://dx.doi.org/10.1016/j.coastaleng.2010.02.006.

Mol, M., Bosboom, J., De Valk, C.F., Reniers, A.J.H.M., Stive, M.J.F., Yuan, J., 2015. The Effective Transport Difference: A New Concept for Morphodynamic Model Validation (M.Sc. thesis). TU Delft, URL http://resolver.tudelft.nl/uuid:aa35b28a-8bca-4b33-b99c-05a79e9154a6.

Monge-Ganuzas, M., Gainza, J., Liria, P., Epelde, I., Uriarte, A., Garnier, R., González, M., Nuez, P., Jaramillo, C., Medina, R., 2017. Morphodynamic evolution of Laida beach (Oka estuary, Urdaibai Biosphere Reserve, southeastern Bay of Biscay) in response to supratidal beach nourishment actions. J. Sea Res. 130, 85–95. http://dx.doi.org/10.1016/j.seares.2017.06.003.

Novaczek, E., Devillers, R., Edinger, E., 2019. Generating higher resolution regional seafloor maps from crowd-sourced bathymetry. PLoS One 14 (6), 1–23. http://dx.doi.org/10.1371/journal.pone.0216792.

Orzech, M.D., Reniers, A.J.H.M., Thornton, E.B., MacMahan, J.H., 2011. Megacusps on rip channel bathymetry: Observations and modeling. Coast. Eng. 58 (9), 890–907. http://dx.doi.org/10.1016/j.coastaleng.2011.05.001.

Pedrozo-Acuña, A., Simmonds, D.J., Otta, A.K., Chadwick, A.J., 2006. On the cross-shore profile change of gravel beaches. Coast. Eng. 53 (4), 335–347. http://dx.doi.org/10.1016/j.coastaleng.2005.10.019.

Plant, N.G., Holland, K.T., Puleo, J.A., Gallagher, E.L., 2004. Prediction skill of nearshore profile evolution models. J. Geophys. Res. Oceans 109 (C1), http://dx.doi.org/10.1029/2003JC001995.

Rachev, S.T., Rüschendorf, L., 1998. Mass Transportation Problems: Volume I: Theory. Springer Science & Business Media, http://dx.doi.org/10.1007/b98893.

van Rijn, L.C., Walstra, D.J.R., Grasmeijer, B.T., Sutherland, J., Pan, S., Sierra, J.P., 2003. The predictability of cross-shore bed evolution of sandy beaches at the time scale of storms and seasons using process-based profile models. Coast. Eng. 47, 295–327. http://dx.doi.org/10.1016/S0378-3839(02)00120-5.

Roelvink, J.A., 2006. Coastal morphodynamic evolution techniques. Coast. Eng. 53 (2–3), 277–287. http://dx.doi.org/10.1016/j.coastaleng.2005.10.015.

Roelvink, D., Reniers, A., van Dongeren, A., van Thiel de Vries, J., McCall, R., Lescinski, J., 2009. Modelling storm impacts on beaches, dunes and barrier islands. Coast. Eng. 56 (11–12), 1133–1152. http://dx.doi.org/10.1016/j.coastaleng.2009.08.006.

Ruessink, B.G., Kuriyama, Y., 2008. Numerical predictability experiments of cross-shore sandbar migration. Geophys. Res. Lett. 35 (1), L01603. http://dx.doi.org/10.1029/2007GL032530.

Ruessink, B.G., Kuriyama, Y., Reniers, A.J.H.M., Roelvink, J.A., Walstra, D.J.R., 2007. Modeling cross-shore sandbar behavior on the timescale of weeks. J. Geophys. Res. Earth Surf. 112 (F3), 2003–2012. http://dx.doi.org/10.1029/2006JF000730.

Ruggiero, P., Walstra, D.J.R., Gelfenbaum, G., van Ormondt, M., 2009. Seasonal-scale nearshore morphological evolution: Field observations and numerical modeling. Coast. Eng. 56 (11–12), 1153–1172. http://dx.doi.org/10.1016/j.coastaleng.2009.08.003.

Santambrogio, F., 2015. Optimal Transport for Applied Mathematicians. Birkäuser, NY, pp. 99–102. http://dx.doi.org/10.1007/978-3-319-20828-2.

Scott, T.R., Mason, D.C., 2007. Data assimilation for a coastal area morphodynamic model: Morecambe Bay. Coast. Eng. 54 (2), 91–109. http://dx.doi.org/10.1016/j.coastaleng.2006.08.008.

Simmons, J.A., Harley, M.D., Marshall, L.A., Turner, I.L., Splinter, K.D., Cox, R.J., 2017. Calibrating and assessing uncertainty in coastal numerical models. Coast. Eng. 125, 28–41. http://dx.doi.org/10.1016/j.coastaleng.2017.04.005.

Simmons, J.A., Splinter, K.D., Harley, M.D., Turner, I.L., 2019. Calibration data requirements for modelling subaerial beach storm erosion. Coast. Eng. 152, 103507. http://dx.doi.org/10.1016/j.coastaleng.2019.103507.

Sutherland, J., Peet, A.H., Soulsby, R.L., 2004. Evaluating the performance of morphological models. Coast. Eng. 51 (8–9), 917–939. http://dx.doi.org/10.1016/j.coastaleng.2004.07.015.

Taylor, K.E., 2001. Summarizing multiple aspects of model performance in a single diagram. J. Geophys. Res.: Atmos. 106 (D7), 7183–7192. http://dx.doi.org/10.1029/2000JD900719.

van der Wegen, M., Jaffe, B.E., Roelvink, J.A., 2011. Process-based, morphodynamic hindcast of decadal deposition patterns in San Pablo Bay, California, 1856–1887. J. Geophys. Res. 116 (F2), F02008. http://dx.doi.org/10.1029/2009JF001614.

Villani, C., 2003. Topics in Optimal Transportation. (58), American Mathematical Soc., URL https://bookstore.ams.org/gsm-58/.

Walstra, D.J.R., Reniers, A.J.H.M., Ranasinghe, R., Roelvink, J.A., Ruessink, B.G., 2012. On bar growth and decay during interannual net offshore migration. Coast. Eng. 60, 190–200. http://dx.doi.org/10.1016/j.coastaleng.2011.10.002.

van der Wegen, M., Roelvink, J., 2012. Reproduction of estuarine bathymetry by means of a process-based model: Western Scheldt case study, the Netherlands. Geomorphology 179, 152–167. http://dx.doi.org/10.1016/j.geomorph.2012.08.007.

Williams, J.J., de Alegrí a Arzaburu, A.R., McCall, R.T., van Dongeren, A., 2012. Modelling gravel barrier profile response to combined waves and tides using XBeach: Laboratory and field results. Coast. Eng. 63, 62–80. http://dx.doi.org/10.1016/j.coastaleng.2011.12.010.

Williams, C.N., Cornford, S.L., Jordan, T.M., Dowdeswell, J.A., Siegert, M.J., Clark, C.D., Swift, D.A., Sole, A., Fenty, I., Bamber, J.L., 2017. Generating synthetic fjord bathymetry for coastal greenland. Cryosphere 11 (1), 363–380. http://dx.doi.org/10.5194/tc-11-363-2017.